



Ultrasonic and seismic constraints on crystallographic preferred orientations of the Priestley Glacier shear margin, Antarctica

Franz Lutz¹, David J. Prior¹, Holly Still², M. Hamish Bowman¹, Bia Boucinhas³, Lisa Craw⁴, Sheng Fan¹, Daeyeong Kim⁵, Robert Mulvaney⁶, Rilee E. Thomas¹, and Christina L. Hulbe²

¹Department of Geology, University of Otago, Dunedin, New Zealand

²School of Surveying, University of Otago, Dunedin, New Zealand

³Antarctica New Zealand, Christchurch, New Zealand

⁴Institute for Marine and Antarctic Sciences, University of Tasmania, Hobart, TAS, Australia

⁵Division of Earth Sciences, Korea Polar Research Institute, Incheon, Republic of Korea

⁶British Antarctic Survey, Natural Environment Research Council, Cambridge, United Kingdom

Correspondence: Franz Lutz (franz.lutz@otago.ac.nz)

Abstract. Crystallographic preferred orientations (CPOs) are particularly important in controlling the mechanical properties of glacial shear margins. Logistical and safety considerations often make direct sampling of shear margins difficult and geophysical measurements are commonly used to constrain the CPOs. We present here the first direct comparison of seismic and ultrasonic data with measured CPOs in a polar shear margin. The measured CPO from ice samples from a 58 m deep borehole in the left lateral shear margin of the Priestley Glacier, Antarctica, is dominated by horizontal c-axes aligned sub-perpendicular to flow. A vertical seismic profile experiment with hammer shots up to 50 m away from the borehole, in four different azimuthal directions, shows velocity anisotropy of both P-waves and S-waves. Matching P-wave data to the anisotropy corresponding to CPO models defined by horizontally aligned c-axes gives two possible solutions for c-axis azimuth, one of which matches the c-axis measurements. If both P-wave and S-wave data are used, there is one best fit for azimuth and intensity of c-axis alignment that matches well the measurements. Azimuthal P-wave and S-wave ultrasonic data recorded in the laboratory on the ice core show clear anisotropy that matches that predicted from the CPO of the samples. With good quality data, azimuthal increments of 30° or less will constrain well the orientation and intensity of c-axis alignment. Our experiments provide a good framework for planning seismic surveys aimed at constraining the anisotropy of shear margins.

1 Introduction

Ice streams and glaciers form localised regions of high ice flow velocity inside otherwise mostly stationary ice masses of Antarctica and Greenland (Truffer and Echelmeyer, 2003) and play a key role in the mass balance of polar ice masses. As result of high flow velocities, the margins of these streaming ice bodies undergo large strain as they are in contact with stationary ice or rock. Crystallographic preferred orientation (CPO) patterns inside glacier margins have been found to indicate a very high degree of crystal alignment in the horizontal direction (Jackson and Kamb, 1997; Monz et al., 2021; Gerbi et al., 2021; Thomas et al., 2021). These results are consistent with observations from shear deformation experiments of ice where c-axis maxima are always aligned perpendicular to the shear plane (Bouchez and Duval, 1982; Qi et al., 2019; Journaux et al., 2019).



The presence of a CPO results in anisotropic mechanical properties and so influences the viscous behaviour of ice significantly (Azuma and Goto-Azuma, 1996; Budd et al., 2013; Faria et al., 2014; Hudleston, 2015). Shear margins of glaciers are therefore expected to affect the character of ice flow in ice streams due to their distinct mechanical properties (Minchew et al., 2018; Hruby et al., 2020; Drews et al., 2021). The advection of the shear margins during the flow of ice from land to sea can result in bands of strongly deformed ice that transect ice shelves (LeDoux et al., 2017) and can potentially affect the stability of ice shelves. Modelling suggests that remnant CPO resultant in shear margins can be present 10000 years after advection downstream (Lilien et al., 2021).

A better understanding of CPO patterns in glacier shear margins is therefore highly desirable to accurately represent their mechanical properties. Ice core drilling, the primary direct information source for CPO, is however rarely performed on fast-flowing ice because of difficulties in access and on site safety. Geophysical studies, e.g. seismic (Bentley, 1971; Blankenship and Bentley, 1987; Picotti et al., 2015; Vélez et al., 2016) or radar (Matsuoka et al., 2003; Jordan et al., 2020; Ershadi et al., 2021) surveys provide an alternative way of constraining bulk CPO. Ideally, geophysical work should be combined with drilling, to recover ice samples for microstructure analysis, and so enable a cross-calibration of CPO constraints.

A continuous ice core of 58 m length was drilled and recovered in December 2019 and January 2020 (Thomas et al., 2021) in a lateral shear margin of the Priestley Glacier, located in Victoria Land, Antarctica, see Figure 1(a). At the site the glacier is ~ 1000 m thick and 8 km wide (Frezzotti et al., 2000). Ice flow velocities are measured to increase from ~ 45 m/year close to the glacier margin to ~ 130 m/year towards the center (Mouginot et al., 2019; Thomas et al., 2021), resulting in strong shear kinematics. Core samples were analysed for CPO using electron backscatter diffraction (EBSD) measurements (Thomas et al., 2021) and a strong horizontal clustering of c-axes was observed throughout the entire length of the core. The core orientation was carefully preserved during drilling which enabled the placement of CPO orientation relative to the macroscopic ice kinematics.

After completion of drilling and core retrieval, the open borehole was used to conduct a vertical seismic profile (VSP) experiment to constrain seismic properties of the near-surface glacier ice, with a particular focus on seismic anisotropy. To complete the link between seismic anisotropy of the ice volume around the borehole and CPO measurements from the core, multiazimuthal ultrasonic velocity measurements (Langway et al., 1988; Hellmann et al., 2021) were made on core samples in the laboratory.

This study presents the first of its kind to explicitly study the very specific Horizontal Cluster CPO type observed in shear margins with seismic methods. Analyses of seismic, ultrasonic and measured CPO datasets are combined to assess the potential of active source seismic surveys for the constraint of shear margin anisotropy.

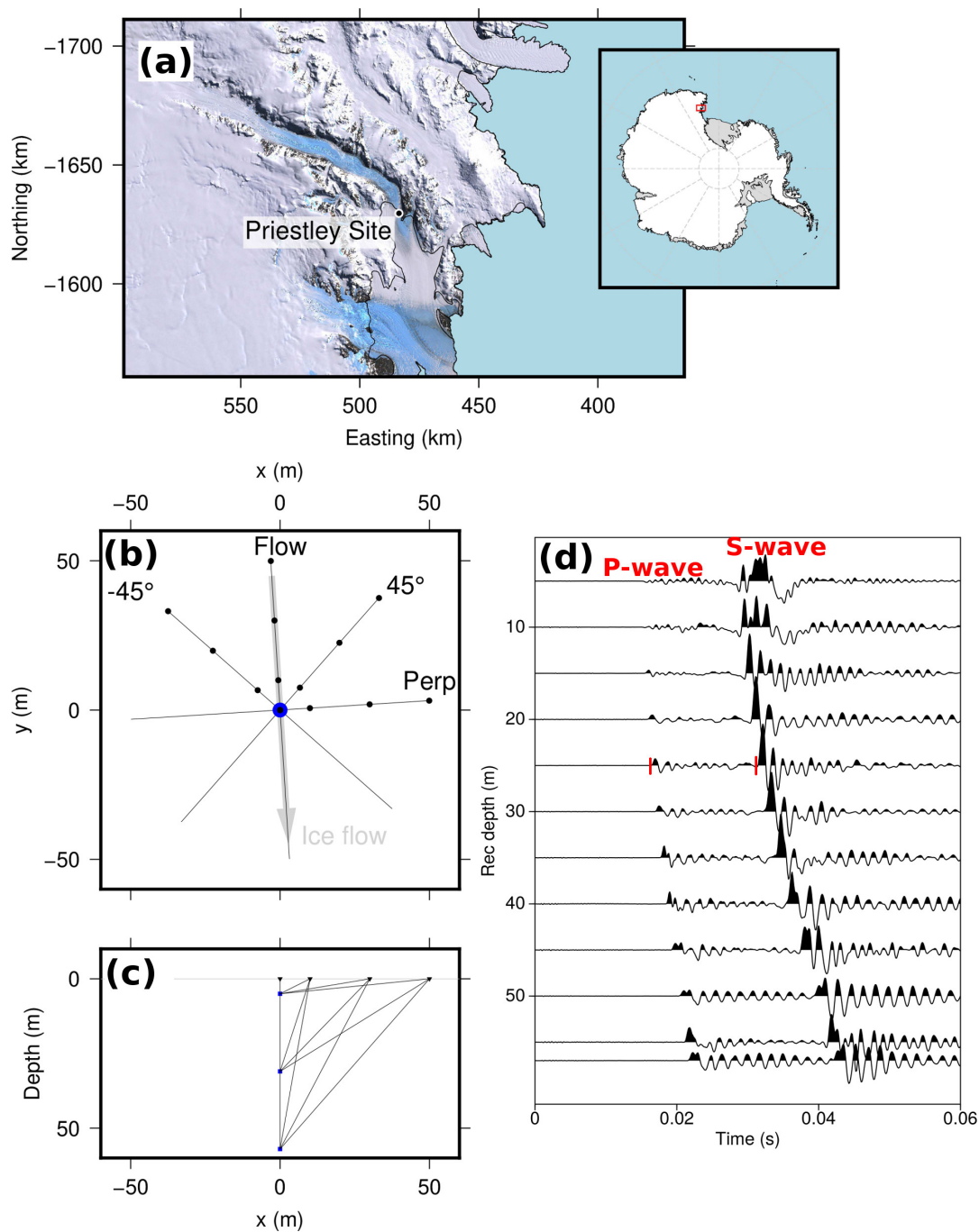


Figure 1. (a) Regional map of the Priestley Glacier site. Coordinates are given by the polar stereographic projection with latitude of true scale at -71°S . Landsat Image courtesy of USGS. (b) Map view illustration of VSP geometry. Black markers show shot point locations, the borehole location is shown in blue. (c) Cross-section illustration of VSP geometry showing the surface shotpoints in black and three borehole seismometer positions in blue. (d) Vertical component traces of borehole seismometer for shots at 50 m offset along the 45° -profile. Example P- and S-wave arrival time picks are shown at 25 m depth as red vertical lines.



2 Seismic anisotropy informed by a vertical seismic profile shooting

2.1 Data acquisition

A VSP dataset was recorded at the Priestley drill site using a borehole seismometer (built by ESS Earth Sciences, Victoria, Australia) with a pneumatic clamping system which was installed in depths z between 5 m and 57 m below the glacier surface. The suspension cable, to the centre of the seismometer, remained close to the centre of the hole at the surface for all seismometer depths indicating true verticality of the borehole. Signals from a hammer-and-plate source were recorded using a Geometrics Geode for a walkaway-VSP geometry along four profiles with different azimuths, where shots were placed at offsets x of 0 m (“Zero-offset” geometry), 10 m, 30 m and 50 m from the top of the borehole. Profile names (“Flow“, ”Perp“, “45“, “-45”) indicate their orientation relative to the glacier flow direction (see Table 1). The survey geometry is illustrated in Figure 1(b). The depth increments of the borehole seismometer along the four profiles are shown in Table 1.

Table 1. Multi-azimuth VSP survey parameters.

Shot profile orientation (Profile name)	Seismometer depth increment (m)
Zero-offset	1
Flow-parallel (“Flow”)	1
Flow-perpendicular (“Perp”)	2.5
45° to flow (“45”)	5
-45° to flow (“-45”)	5

Data recording for each shot in the field was initiated by a Geometrics switch trigger taped to the sledgehammer handle. Quality control of traces in the field found that this trigger type produces inconsistent zerotimes and the recorded signal from surface geophones collocated at the shot points were used to define shot times. The Geode was set to record 100 ms before the hammer switch trigger signal to allow manual picking of the first-arrival time on the shotpoint surface geophone, which corresponds to the time of hammer impact. Total recording length was 2 s with a sampling interval of 0.125 ms. Shot and geophone locations were cleared of all snow cover to ensure direct contact of source and receivers to the hard ice surface. Several repeat shots were recorded at all shot points along a given profile for one seismometer depth before the instrument was lowered to the next depth. After all shots for all seismometer depths were completed for a profile, surface geophones were moved to the next profile position.

Polarisation patterns indicate a ringing effect of the pneumatic borehole seismometer, where phase arrivals are followed by a tail of mono-frequent oscillations (see traces in Figure 1(d)). The oscillations are distributed along all three seismometer components and therefore it was found that a separation of P- and S-wave signals through component rotation into ray coordinates (Wüstefeld et al., 2010) is not achievable in the VSP dataset. This precludes investigating polarisation patterns, such as S-wave splitting, as a constraint on seismic anisotropy (Lutz et al., 2020).



75 2.2 Multi-azimuth VSP traveltimes

P- and S-wave first arrival signals were recorded with high signal-to-noise ratio and phase arrival times can be clearly identified. Picking of seismic phase arrivals is performed manually for each shot to determine traveltimes: one first arrival pick is made on the surface geophone trace at the shot location in addition to picks of P- and S-wave arrivals on the borehole seismometer traces. The P- and S-wave traveltime t is then calculated as the difference between the picked arrival time on the borehole
80 seismometer and the picked source time on the surface geophone.

Observed P-wave traveltimes along the seismic profiles are presented in Figure 2(a)-(d). The zero-offset P-wave traveltimes in Figure 2(a) can be approximated by a constant velocity model ($v_P = 3850$ m/s, solid line). This highlights that there is little velocity variation due to heterogeneity in the shallow glacier ice.

Differences in traveltimes between the profiles become apparent for shots at offsets ≥ 30 m and below seismometer depths
85 of ~ 25 m. The Flow- and -45° -profiles show consistently earlier P-wave arrivals than the Perp- and 45° -profiles.

Observed S-wave traveltimes are presented in Figure 2(f)-(h) for shots from the four wakaway VSP profiles. Signal-to-noise ratios from zero-offset shots were found to be insufficient to allow picking of S-wave arrivals. The first indication of S-wave arrivals was picked consistently, traveltimes are therefore interpreted to be representative of the fast S-wave velocity v_{S1} and will be consistently referred to as fast S-wave properties throughout this study. Systematic traveltime differences between
90 profiles are observed particularly for shots from 50 m offset, where the -45° -profile shows the earliest arrival times over almost the entire depth range. Only for seismometer depths below 50 m are traveltimes from the Perp-profile measured at the same times or earlier than traveltimes from along the -45° -profile. The Flow- and 45° -profiles show similar traveltimes that are registered later than the traveltimes along the other profiles.

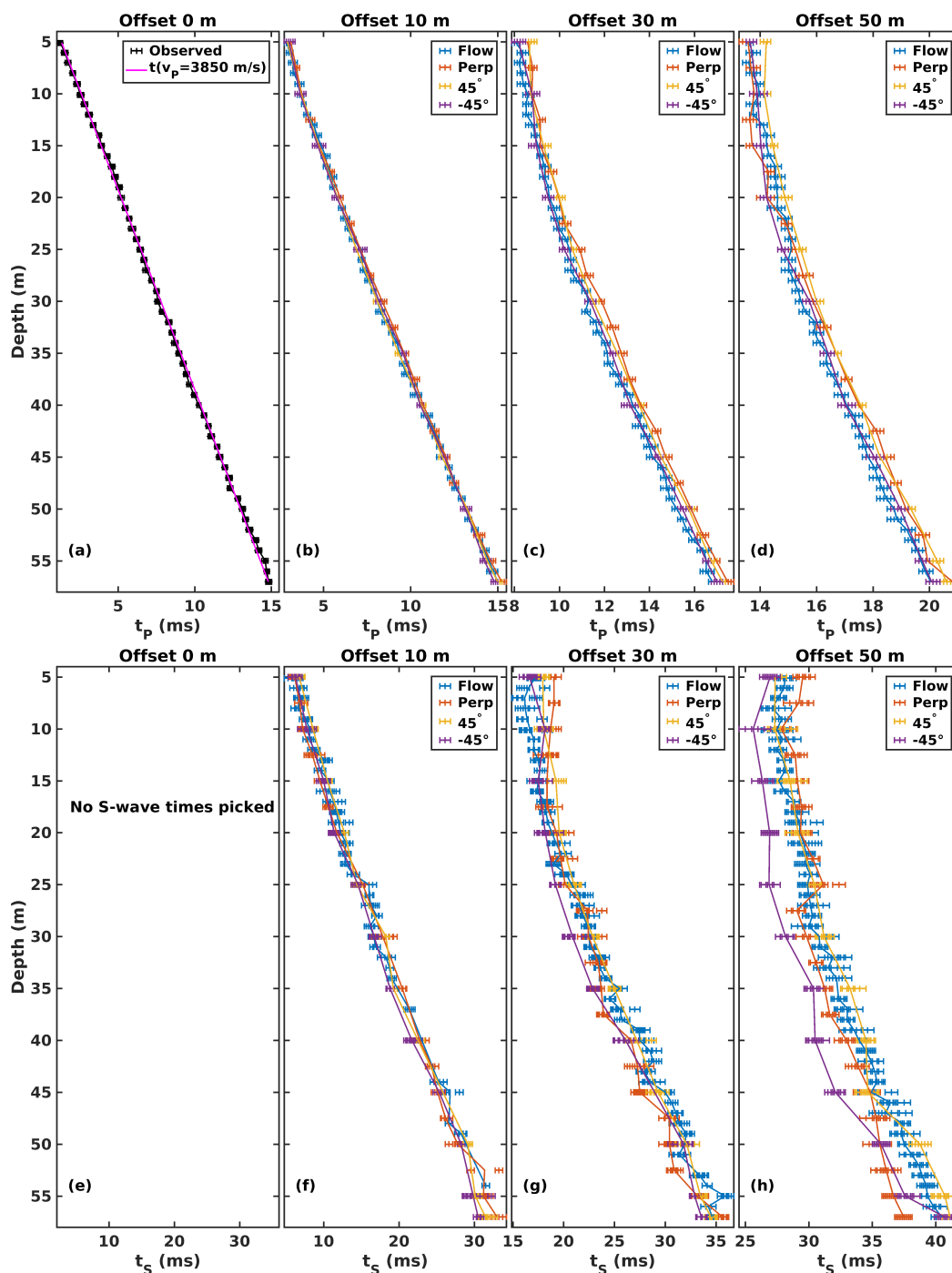


Figure 2. VSP traveltimes observed along the four shot profiles. (a) P-wave traveltimes for shots from 0 m offset. (b) P-wave traveltimes for shots from 10 m offset. (c) P-wave traveltimes for shots from 30 m offset. (d) P-wave traveltimes for shots from 50 m offset. (e) No S-wave traveltimes were picked from 0 m offset shots due to poor signal-to-noise-ratio. (f) S-wave traveltimes for shots from 10 m offset. (g) S-wave traveltimes for shots from 30 m offset. (h) S-wave traveltimes for shots from 50 m offset.



2.3 Velocity anisotropy

95 Seismic velocities are calculated using Equation (1) from the presented traveltimes for different depths z , offsets x and azimuths in Figure 2.

$$v = \frac{\sqrt{x^2 + z^2}}{t} \quad (1)$$

The calculation is based on the assumption of straight raypaths between shot and receiver, which is regarded as valid approximation for a site location on hard ice without snow cover. The seismic waves travel entirely in ice and no large velocity gradients

100 that could result in significant raypath bending are therefore expected (Gusmeroli et al., 2013). The zero-offset traveltimes in Figure 2(a) exhibit no apparent indications of velocity gradients since they can be approximated by a constant vertical P-wave velocity. The incidence angle θ from the vertical direction is defined by Equation (2).

$$\theta = \arctan\left(\frac{x}{z}\right) \quad (2)$$

Velocity uncertainties Δv are calculated using Equation 3 from uncertainty estimates for P-wave traveltime $\Delta t_P = 0.125$ ms, 105 S-wave traveltime $\Delta t_S = 1$ ms, offset $\Delta x = 0.2$ m and depth $\Delta z = 0.1$ m. Observations with relative uncertainty $\Delta v/v > 0.05$ are discarded from further analysis. The range of observed velocities along the different shot profiles is presented in Table 2.

$$\Delta v = \frac{2x\Delta x + 2z\Delta z}{t \cdot \sqrt{x^2 + z^2}} + \frac{\Delta t \cdot \sqrt{x^2 + z^2}}{t^2} \quad (3)$$

Table 2. Walkaway VSP velocities.

Profile	Min v_P (m/s)	Max v_P (m/s)	Min v_S (m/s)	Max v_S (m/s)
Flow	3594 ± 158	4009 ± 100	1632 ± 77	2016 ± 77
Perp	3484 ± 98	3923 ± 62	1580 ± 63	2050 ± 40
45°	3427 ± 96	3953 ± 101	1678 ± 70	1971 ± 42
−45°	3514 ± 98	4006 ± 198	1733 ± 72	2119 ± 47



3 Seismic anisotropy informed by ultrasonic experiments

Ultrasonic experiments were performed inside a freezer at temperature $-23 \pm 2^\circ\text{C}$ on a subset of samples from the continuous
110 ice core. Samples were lathed to the shape of a highly regular cylinder. Travelttime measurements were made perpendicular
to the core axis in multiple azimuths to inform ultrasonic velocities in the horizontal direction of the glacier ice. Ultrasonic
P- or S-wave transducers were spring loaded against the cylinder surface, on opposing sides of the cylinder (Figure 3(a)+(b)).
S-wave transducers were used for excitation and recording of S-waves with polarisations in the vertical (parallel to the long
core axis) and horizontal (perpendicular to the long core axis) direction. Coupling of transducers to the ice core samples was
115 ensured through the use of synthetic high-performance low temperature grease.

Travelttime measurements across the ice core were made in azimuthal increments of 10° covering the full core diameter,
resulting in $N = 36$ measurements per transducer arrangement and core. A fiducial line that was made in the field to provide
geographic reference of the core orientation served as the 0° reference on individual samples. The fiducial line was made
perpendicular to the glacier flow direction on the surface (Thomas et al., 2021). New fiducial lines were started wherever a core
120 break could not be fitted together and the relative orientations of the lines reconstructed using the core CPO (Thomas et al.,
2021). Measurements are on core sections 003 from a depth of ~ 2.5 m (diameter $d = 100.6 \pm 0.3$ mm), 007 from a depth of
 ~ 6.0 m (diameter $d = 99.9 \pm 0.3$ mm) and 010 from a depth of ~ 8.5 m (diameter $d = 100.3 \pm 0.3$ mm).

The ultrasonic source signal pulse was created by a JSR Ultrasonics DPR300 Pulser unit and shows a dominant frequency
 $f \approx 1$ MHz, resulting in a dominant wavelength of $\lambda \approx 3.8$ mm in the ice. Recording of the source and receiver signal was
125 performed on separate oscilloscope channels by a PicoScope digital oscilloscope with a sampling rate $t_S = 0.8$ ns. Signals
were recorded directly by the oscilloscope without the use of amplifiers. The source signal was used to trigger signal recording
by exceedance of an amplitude threshold. A signal length of $100 \mu\text{s}$ after triggering is recorded.

3.1 Processing

At each azimuth 64 individual waveforms were recorded. The mean amplitude and linear trend is removed from these individual
130 traces before they are stacked to increase signal-to-noise ratio. The stacked traces are tapered and filtered with a bandpass filter
with corner frequencies $f_1 = 50$ KHz $f_2 = 5$ MHz and normalised for plotting.

Waveforms recorded on sample ~~sample~~ 007 are shown in Figure 3(c)-(e). The core orientation angle in these plots is relative
to the fiducial marker on the core sample. Recorded waveforms using the P-wave transducers are shown in Figure 3(c). A
rotational symmetry with periodicity of 180° is present, which confirms a consistent and reliable excitation and recording of
135 P-wave signals for all azimuths around the core.

Waveforms recorded using S-wave transducers set for vertical vibration are shown in Figure 3(d), indicating a clear period-
icity of 180° and are predominantly indicative of the slow S-wave velocity v_{S2} .

Waveforms from S-wave transducers set for horizontal vibration are shown in Figure 3(e). Here, four local maxima in
velocity are observed for the full range of azimuths. This arrangement of transducers is found to enable the measurement of
140 fast S-wave velocity v_{S1} at most azimuths.

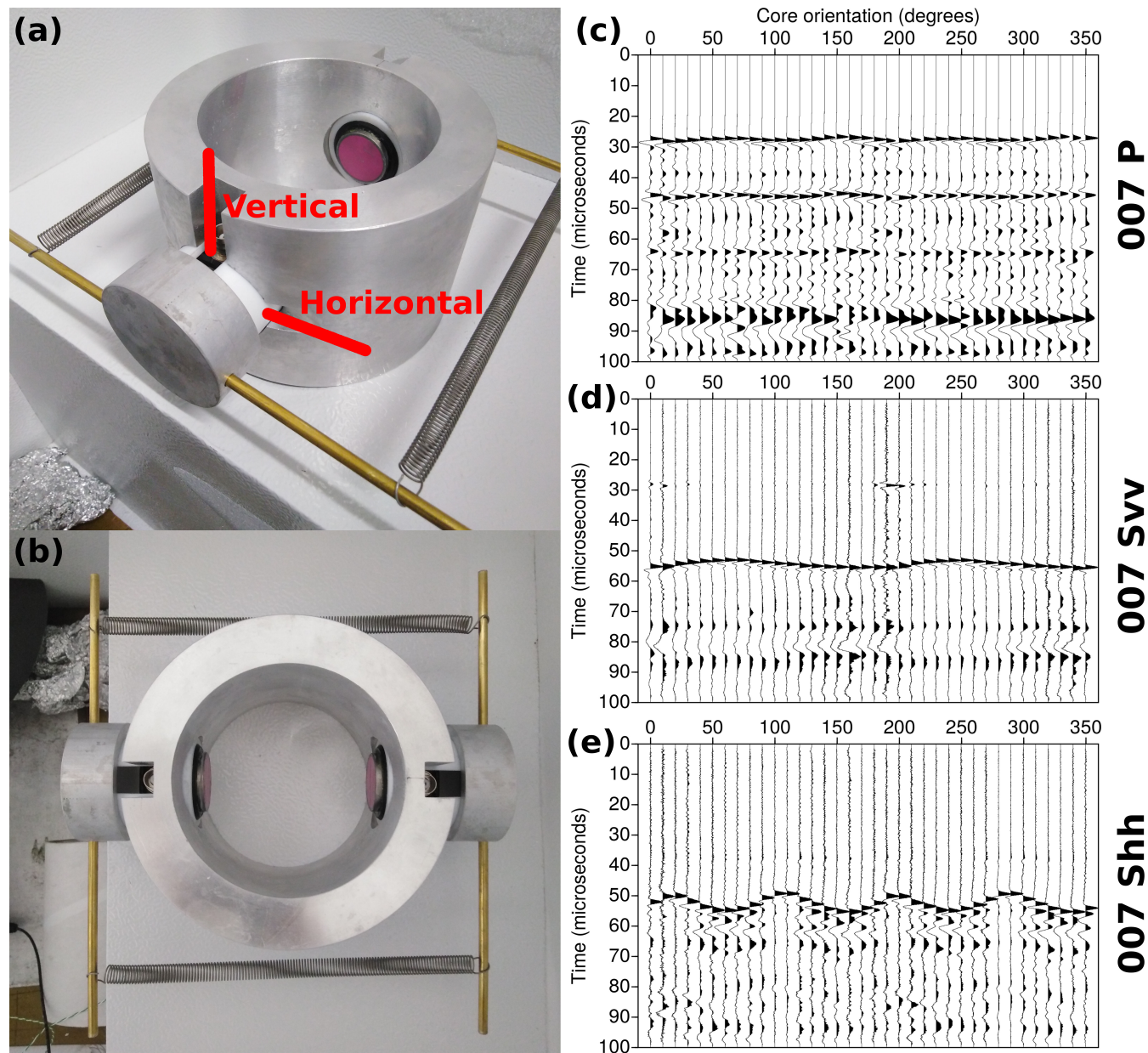


Figure 3. (a) Side view of ultrasonic rig with slots for different transducer orientations highlighted. (b) Map view of ultrasonic rig. Transducers are set for vertical vibration. (c) Multiazimuth signal traces using P-wave transducers on sample 007. (d) Multiazimuth signal traces using S-wave transducers set for vertical vibration on sample 007. (e) Multiazimuth signal traces using S-wave transducers set for horizontal vibration on sample 007.



3.2 P-wave and S-wave ultrasonic velocity results

Arrival times t of the direct P- and S-wave phases are picked by hand on the stacked traces and used to calculate seismic velocities $v = d/t$. Successful measurements of v_P , v_{S1} and v_{S2} are made at all azimuths and samples, which constitutes an unprecedented characterisation of seismic anisotropy in high detail. Velocity uncertainties are calculated from diameter
145 uncertainty $\Delta d = 0.3$ mm and picking uncertainty $\Delta t = 0.1$ μ s.

Ultrasonic P- and S-wave velocities of the three studied core sections are shown in Figure 4(a)-(c). The velocities are presented in the kinematic reference frame, where the angles relative to the fiducial lines on individual samples are transformed to give the orientation relative to glacier flow at the site (Thomas et al., 2021). The azimuth given in the plots presents the angle from the flow-parallel VSP profile in Figure 1(b) in clockwise direction.

150 Ultrasonic v_P measurements were also made along the core axis, sampling the vertical direction also at -23 ± 2 °C. Sample velocities of $v_{P,vert,003} = 3838 \pm 20$, $v_{P,vert,007} = 3822 \pm 15$ and $v_{P,vert,010} = 3842 \pm 18$ again highlight near constant velocity with depth implicit in the zero-offset VSP P-wave traveltimes (Figure 2(a)). The range of vertical v_P is shown in Figure 4(a). The observation that vertical v_P is faster than horizontal v_P for most azimuths is inconsistent with the expected velocities for a Horizontal Cluster CPO and no definite explanation for this observation is available at this point. Potential additional
155 influences on velocities could be given by populations of “oddly” oriented grains (Thomas et al., 2021) that show orientations in the horizontal plane but outside of the c-axis cluster. They could therefore reduce the maximum v_P along the cluster axis, but not affect v_P in the vertical direction. Anisotropy related to preferred bubble shape or aligned cracks could also play a role.

An attempted measurement of v_S in the vertical direction failed, because no clear ultrasonic S-wave signals that allowed traveltimes picking could be recorded in this geometry.

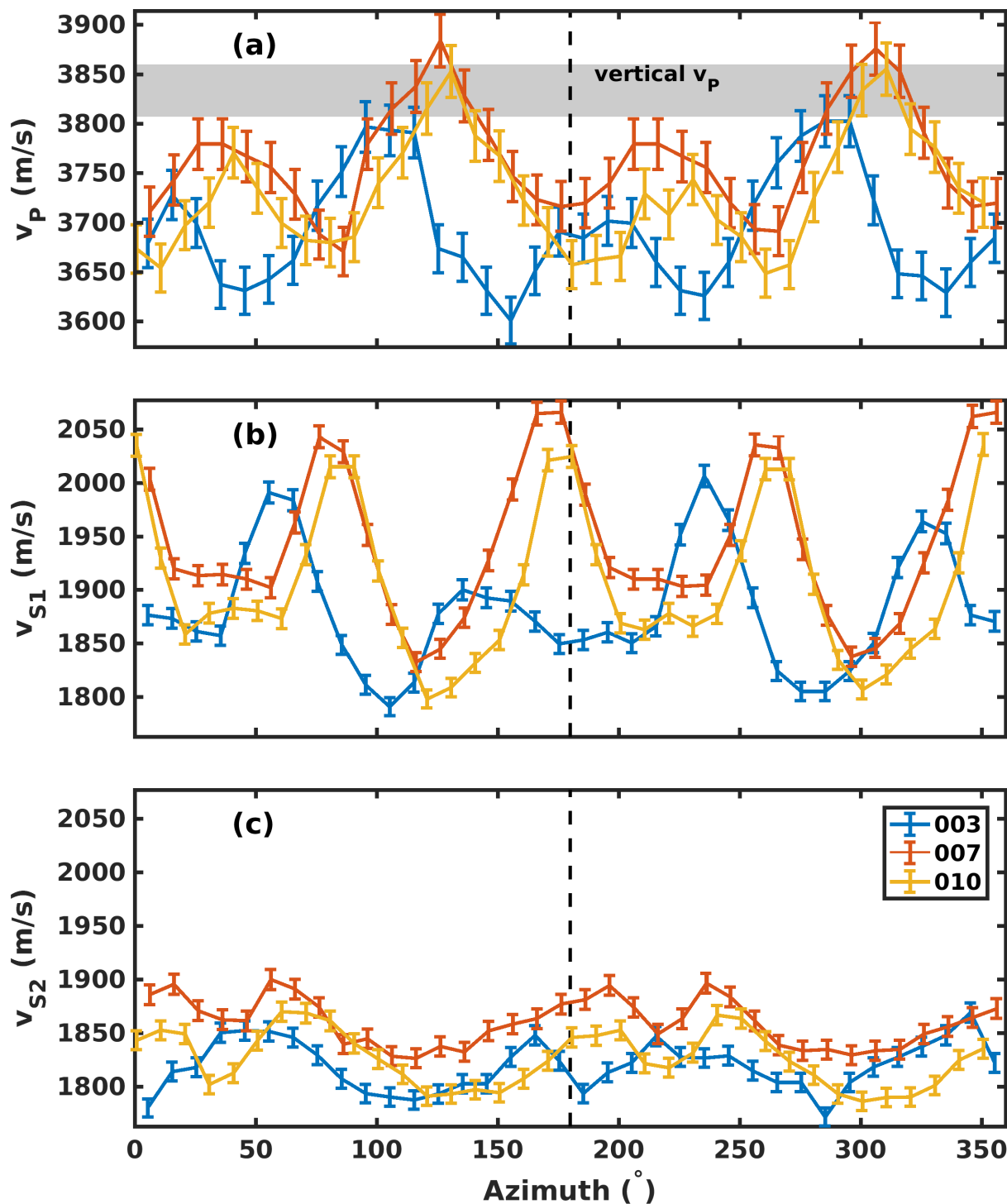


Figure 4. Ultrasonic multi-azimuth velocities for different core sections relative to the macroscopic glacier flow direction (0°). (a) P-wave velocity v_p . The gray-shaded box shows the range of measured vertical ultrasonic v_p . (b) Fast S-wave velocity v_{s1} . (c) Slow S-wave velocity v_{s2} .



160 4 CPO modelling

The observed high degree of seismic anisotropy in VSP seismic and multiazimuth ultrasonic data is consistent with the observation of strong CPO in the retrieved core samples from the site. The availability of constraints from sample microscopic analysis and geophysical data at the Priestley Glacier site is therefore very suitable for a calibration of seismic properties to the known CPO. The observed P- and S-wave velocity anisotropies from VSP and multiazimuth ultrasonic observations are compared to models of polycrystal elasticity connected to CPOs comprising horizontally clustered c-axes. The workflow of matching observed seismic properties to synthetic properties from CPO forward models is a modification of the approach introduced in Lutz et al. (2020).

4.1 Horizontal Cluster CPO

CPO models are created using the MTEX toolbox for Matlab (Mainprice et al., 2011) consisting of 1000 clustered c-axes with cluster symmetry axis in the horizontal direction. A geometrical description of this Horizontal Cluster CPO forward model can be given by a cone with symmetry axis in the horizontal plane that encompasses the clustered c-axes. The model parameters of this cone geometry are defined by the azimuth φ of the cone symmetry axis and the cone opening angle α . An illustration of this CPO type is presented in Figure 5 in an upper-hemisphere stereographic projection.

Seismic properties of individual crystals are characterised by the elasticity tensor C in Equation (4) of synthetic ice at -16°C by Gammon et al. (1983) and density $\rho = 919.1\text{ kg/m}^3$. For any given set of CPO model parameters φ and α , synthetic seismic velocities associated with the CPO are calculated after forming the Voigt-Reuss-Hill-average elastic properties (Hill, 1952; Mainprice, 2007).

$$C = \begin{bmatrix} 13.913 & 7.026 & 5.801 & 0 & 0 & 0 \\ 7.026 & 13.913 & 5.801 & 0 & 0 & 0 \\ 5.801 & 5.801 & 15.059 & 0 & 0 & 0 \\ 0 & 0 & 0 & 3.011 & 0 & 0 \\ 0 & 0 & 0 & 0 & 3.011 & 0 \\ 0 & 0 & 0 & 0 & 0 & 3.4435 \end{bmatrix} \text{ GPa} \quad (4)$$

Model parameters φ and α are systematically varied in regular step sizes and all combinations within the individual parameter ranges presented in Table 3 are explored. Synthetic seismic properties are compared to observations for each model realisation.

4.2 Model misfit calculation

The ability of a CPO model to explain measured seismic anisotropy is assessed by introduction of a misfit between synthetic forward modelled seismic properties and observations. We found that CPO predicted seismic velocities are consistently faster than observed velocities, an effect which can be attributed to the absence of grain boundary effects (Sayers, 2018) or air bubbles

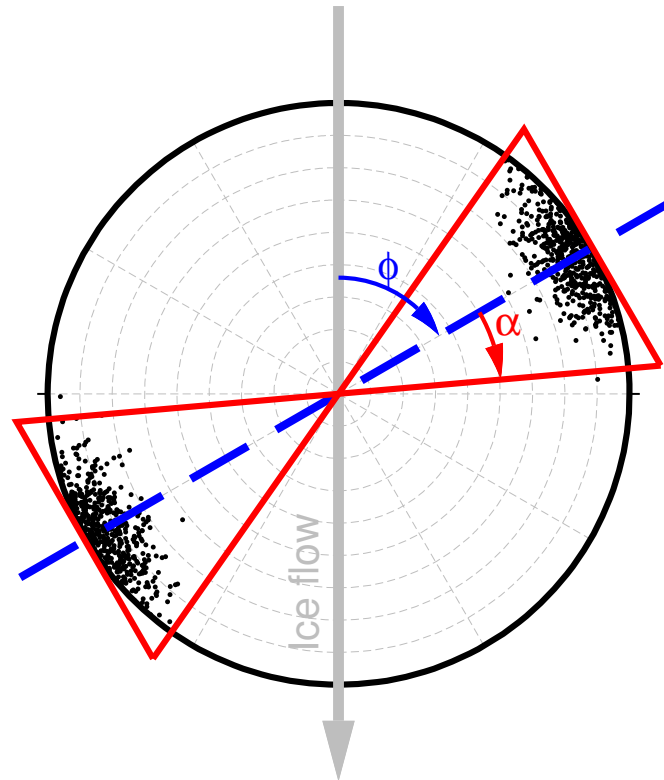


Figure 5. Upper-hemisphere stereographic projection of an example Horizontal Cluster CPO model with illustration of model parameters: Cluster orientation φ and opening angle α .

Table 3. Horizontal Cluster CPO model parameters.

Parameter	Start value	End value	Step size
Cluster orientation φ	0°	180°	5°
Opening angle α	0.1°	40.1°	1°

(Hellmann et al., 2021) in synthetic CPOs. The elasticity tensor by Gammon et al. (1983) was derived using oscillations in GHz frequencies, therefore dispersion is another potential factor to introduce differences between modelled and observed seismic or ultrasonic velocities with Hz to kHz frequencies. Because of these effects, we focus entirely on modelled and observed anisotropic velocity variations rather than absolute velocities, studying the variation of velocities $v(\vartheta)$ along different angles



190 ϑ relative to the mean velocity along all observation angles. This definition of seismic anisotropy δv is given in Equation (5), where \bar{v} is the mean wave velocity of all observations.

$$\delta v = \left(\frac{v}{\bar{v}} - 1 \right) \cdot 100 \quad (5)$$

We consider the elasticity data from Gammon et al. (1983) to provide high accuracy of relative velocity variation. Therefore we have chosen to rely upon these data and no other published elasticities of ice are investigated to match the observed anisotropy, such as done in previous studies which compared absolute measured and synthetic velocities (Diez et al., 2015; Picotti et al., 2015). A misfit χ is calculated by Equation (6) between measured (δv) and synthetic (δv_M) velocity variations. N is the number of velocity observations.

$$\chi(v) = \sqrt{\frac{1}{N} \sum_{i=1}^N (\delta v_i - \delta v_{M,i})^2} \quad (6)$$

Misfits $\chi(v)$ are calculated individually for the v_P , v_{S1} and v_{S2} observations and all synthetic CPO models. The $\chi(v_P)$, $\chi(v_{S1})$ and $\chi(v_{S2})$ misfits are then individually normalised through division by the largest misfit of all models.

4.3 CPO model fit using VSP velocities

The model misfit of the VSP data is calculated using $N_P = 1354$ and $N_{S1} = 1036$ velocity observations. Figure 6(a) shows the normalised misfit values for all models using P-wave velocities $\chi(v_P)$. The best-fitting model is indicated by the red dot and this model CPO is shown in Figure 6(d). Figures 6(b) and 6(e) show S-wave misfits $\chi(v_{S1})$ and the corresponding best-fitting CPO model. The sum of misfits $\chi(v_P)$ and $\chi(v_{S1})$ is presented in 6(c), with its best-fitting CPO model presented in Figure 6(f). Parameters of the best-fitting CPO models using the VSP observations are provided in Table 4. Parameter uncertainties are taken from the range of models that produce the minimum 1% of misfits.

Table 4. Best-fitting CPO model parameters and uncertainties informed by VSP data.

Misfit type	Cluster orientation φ ($^\circ$)	Cluster width α ($^\circ$)	Misfit
$\chi(v_P)$	65 [65,70]	2.1 [0.1,9.1]	0.69 [0.70]
$\chi(v_{S1})$	110 [105,115]	22.1 [19.1,26.1]	0.58 [0.59]
$\sum \chi$	115 [110,115]	18.1 [16.1,24.1]	0.66 [0.66]

Figure 7 shows the observed P-wave anisotropy δv_P along the four survey profiles together with predicted anisotropy from the three best-fitting CPO models in Figure 6. Modelled anisotropies (dashed lines) generally match observations (symbols) within uncertainties along the Flow-, Perp- and -45° profiles. It is notable that the three different models exhibit very similar

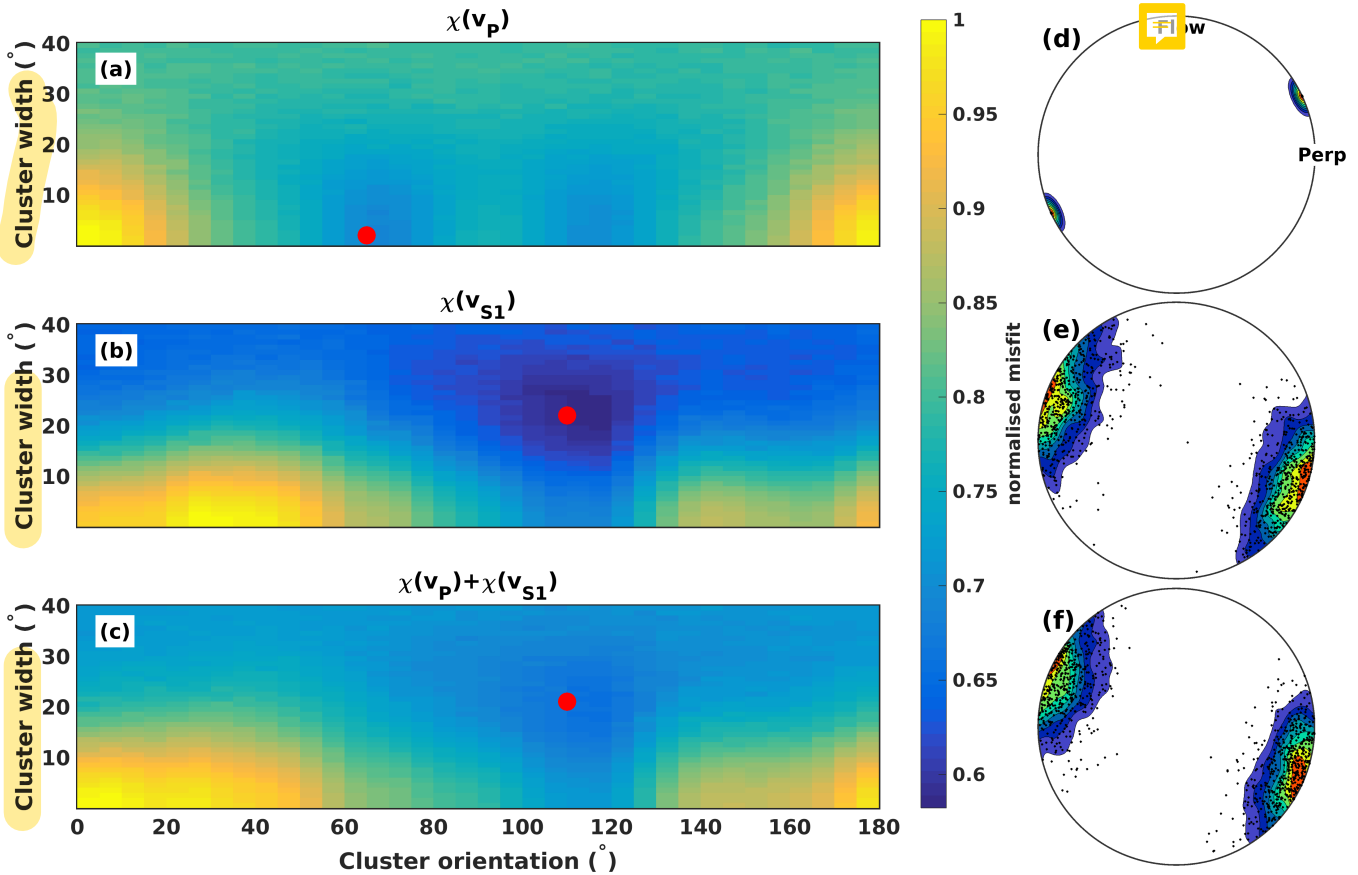


Figure 6. (a) Misfit surface considering only P-wave velocities. (b) Misfit surface considering only S-wave velocities. (c) Misfit surface considering P- and S-wave velocities. (d) Best-fitting CPO model result considering only P-wave velocities. Labels indicate the orientation of the “Flow” and “Perp” profile shots in the VSP survey (compare Figure 1(b)). (e) Best-fitting CPO model result considering only S-wave velocities. (f) Best-fitting CPO model result considering P- and S-wave velocities.

seismic properties along these profiles, although the CPO model informed by $\chi(v_P)$ in Figure 6(d) shows a fundamentally different geometry than the CPO models informed by $\chi(v_{S1})$ or $\chi(v_P) + \chi(v_{S1})$ in Figures 6(e)+(f). The -45° profile shows a larger difference between the models with a steady decrease in δv_P predicted by the models informed by $\chi(v_{S1})$ and $\chi(v_P) + \chi(v_{S1})$, while the $\chi(v_P)$ CPO model suggests a decrease of δv_P to incidence angles of $\sim 40^\circ$, followed by increasing δv_P towards larger incidence angles. The difference between data and models is largest along this profile, however the observed δv_P support the steady decrease of P-wave velocity between vertical (0°) and horizontal incidence (90°) that is suggested by the $\chi(v_{S1})$ and $\chi(v_P) + \chi(v_{S1})$ CPO models.

Fast S-wave anisotropy δv_{S1} observations are shown in Figure 8 alongside the modelled anisotropy. Again, observations and models are all in general agreement on the Flow and Perp profile, albeit an observed decrease in δv_{S1} on the Perp profile



220 for incidence angles $\geq 60^\circ$ which is not satisfyingly matched by any model. The most significant differences are seen along
the 45° and -45° profile, here only the models informed by $\chi(v_{S1})$ and $\chi(v_P) + \chi(v_{S1})$ match observations, while the model
informed by $\chi(v_P)$ is strongly mismatched.

The acquisition geometry of the VSP survey has to be regarded critically, since two profiles (Flow and Perp) show signals
of anisotropy that can ambiguously be explained by CPO models that have fundamentally different cluster geometries. Only
225 the incorporation of diagonal profiles and especially the combination of P- and S-wave information is able to rule out the
unrealistic CPO model informed by $\chi(v_P)$.

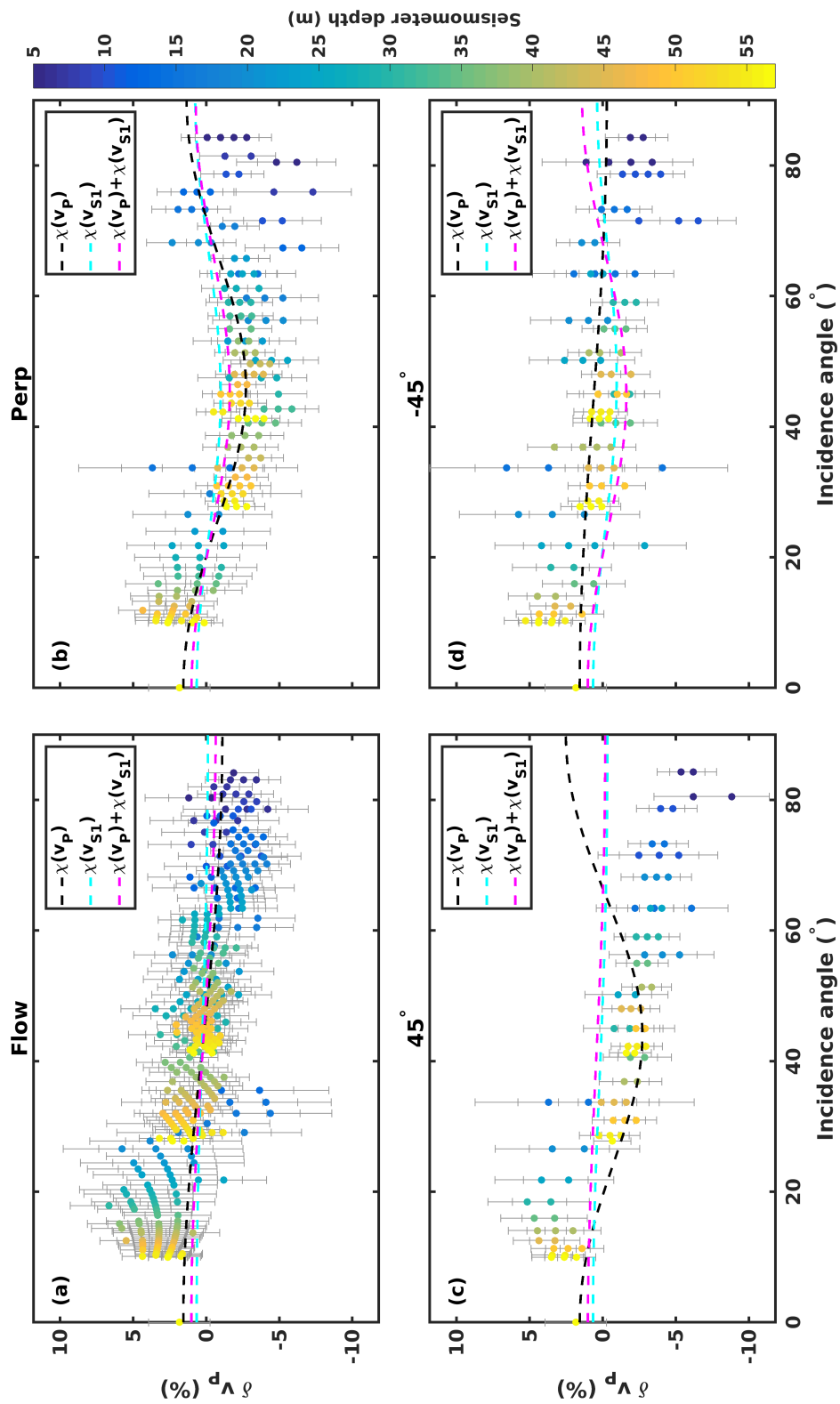


Figure 7. Multi-azimuth P-wave observed velocity anisotropy (symbols) and model results (dashed lines) along the different profiles. (a) Flow-profile (b) Perp-profile (c) 45°-profile (d) -45°-profile

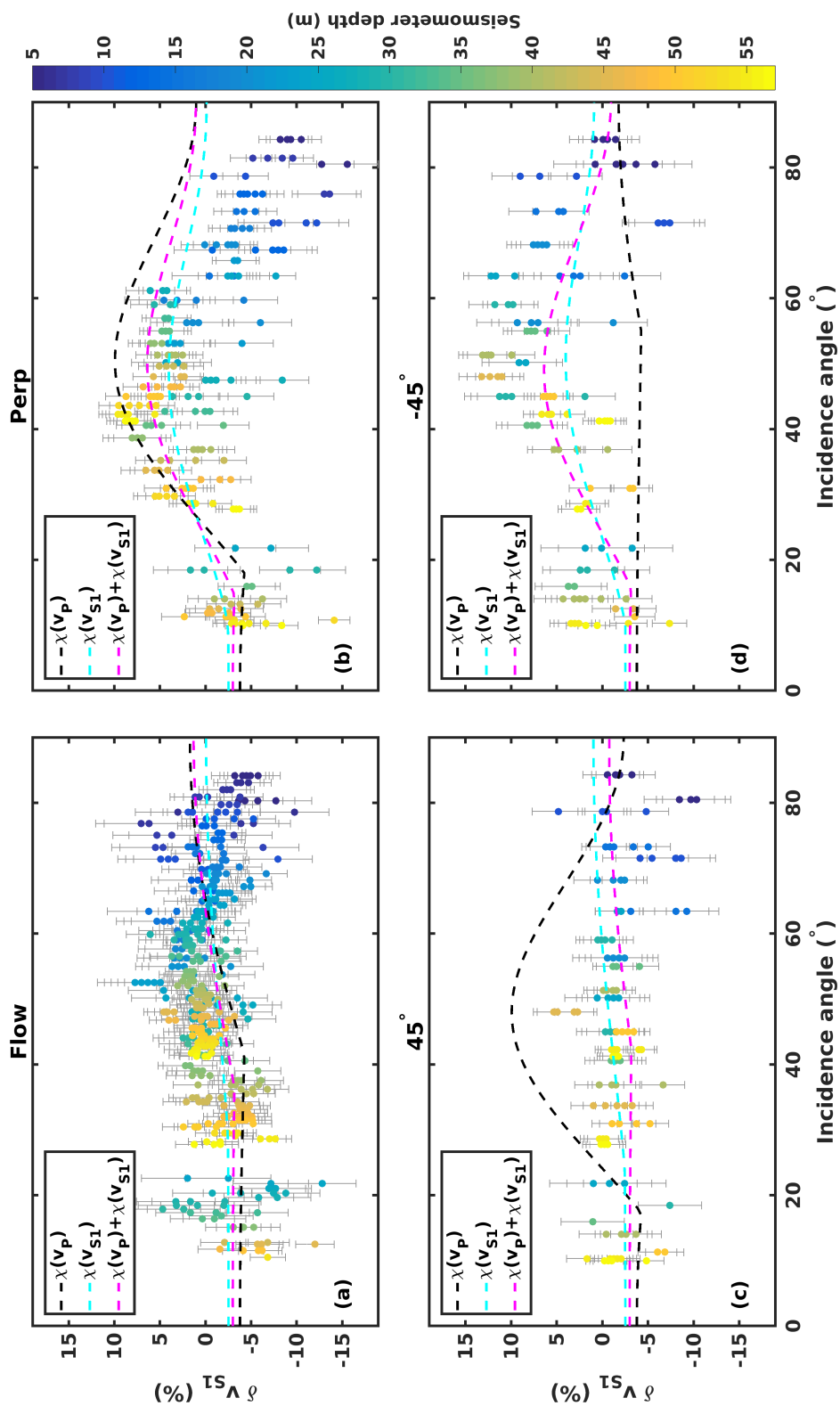


Figure 8. Multi-azimuth S-wave observed velocity anisotropy (symbols) and model results (dashed lines) along the different profiles. (a) Flow-profile (b) Perp-profile (c) 45°-profile (d) -45°-profile



4.4 CPO model fit using ultrasonic velocities

Misfits χ of the Horizontal Cluster CPO are calculated from the multiazimuth observations of v_P , v_{S1} and v_{S2} on the core samples 003, 007 and 010.

230 Figure 9 shows misfits χ of the different velocities for sample 003, where the red mark indicates the best-fitting model. The individual misfits in Figures 9(a)-(c) and the sum of all misfits in Figure 9(d) show best-fitting models with a consistent cluster orientation and a small scatter in reconstructed cluster opening angles. The shape of the areas of lowest misfit shows that cluster orientation can be constrained with higher confidence than cluster width. An overview of CPO model parameters informed by the ultrasonic measurements is provided in Table 5. The misfit informed by v_{S1} in Figure 9(b) shows a side minimum at an
 235 orientation that is $\sim 90^\circ$ offset from the best-fitting model. This reflects the shape of the measured v_{S1} variation with azimuth which shows an approximate 90° periodicity, whereas v_P and v_{S2} show 180° periodicity (see Figure 4). The sum of all misfits (Figure 9(d)) is regarded to provide the most reliable constraint on model fit. Here, the side minimum present in $\chi(v_{S1})$ is attenuated which resolves the ambiguity in the CPO model constraint.

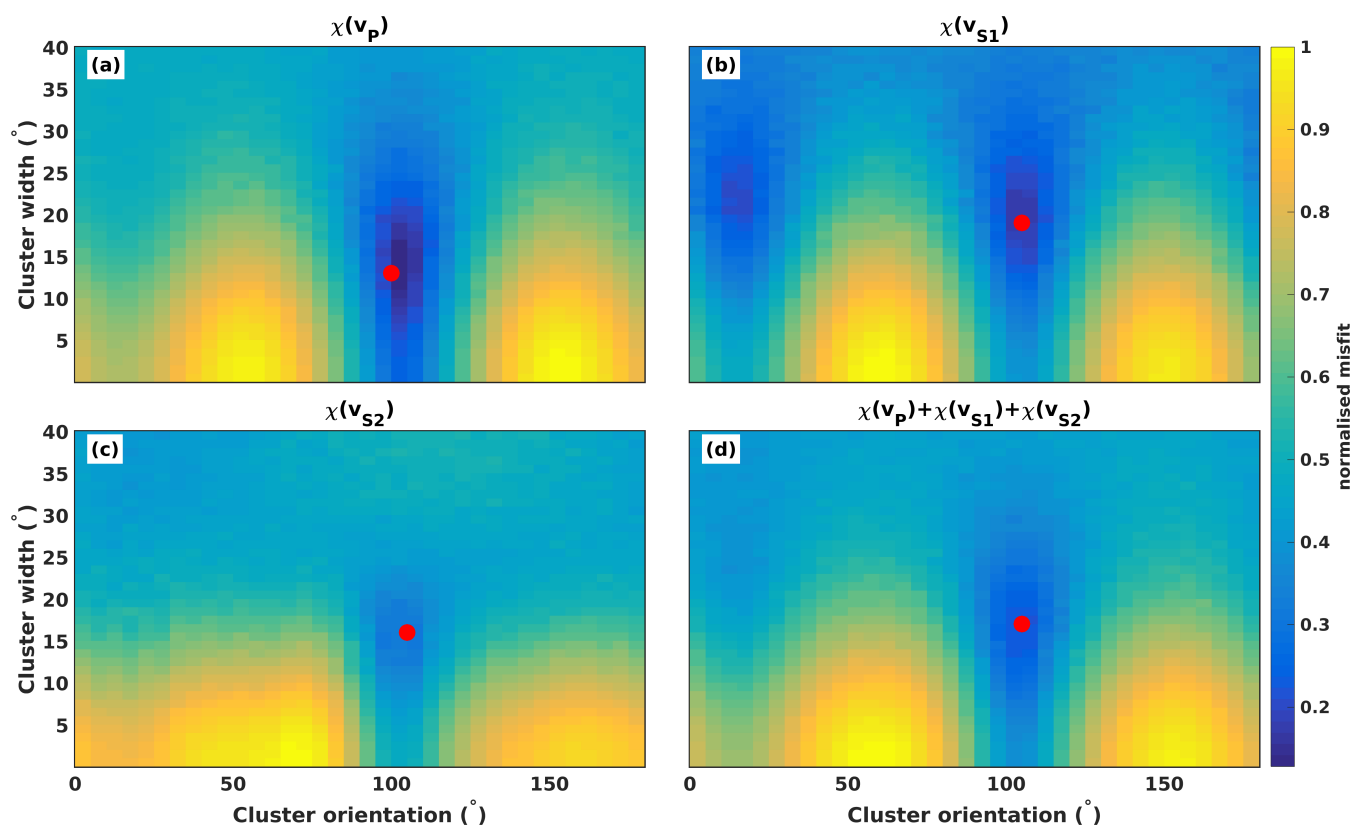


Figure 9. Misfit surfaces of seismic velocities showing fit to model parameters of the Horizontal Cluster CPO for sample 003: (a) $\chi(v_P)$ (b) $\chi(v_{S1})$ (c) $\chi(v_{S2})$ (d) $\chi(v_P) + \chi(v_{S1}) + \chi(v_{S2})$



Table 5. Best-fitting CPO model parameters and uncertainties informed by ultrasonic data.

Misfit type / sample	Cluster orientation φ ($^{\circ}$)	Cluster width α ($^{\circ}$)	Misfit
$\chi(v_P)$ (003)	100 [100,105]	13.1 [9.1,18.1]	0.13 [0.17]
$\chi(v_{S1})$ (003)	105 [100,105]	19.1 [16.1,23.1]	0.18 [0.20]
$\chi(v_{S2})$ (003)	105 [95,105]	16.1 [12.1,18.1]	0.31 [0.33]
$\sum\chi$ (003)	105 [100,105]	17.1 [13.1,20.1]	0.22 [0.24]
$\sum\chi$ (007)	125 [120,130]	14.1 [10.1,19.1]	0.16 [0.22]
$\sum\chi$ (010)	130 [125,135]	14.1 [8.1,18.1]	0.16 [0.22]

The best-fitting models of the three core samples are identified by the minimum in the misfit sum $\chi(v_P) + \chi(v_{S1}) + \chi(v_{S2})$.
 240 The c-axes distribution of these CPO models are shown in upper hemisphere plots in Figure 10 alongside the measured CPO of the samples.

Measured and modelled CPO of sample 003 show excellent agreement, however for samples 007 and 010 the modelled CPO clusters are slightly rotated in clockwise direction relative to the measured CPO geometry. A comparison of observed and forward modelled velocity variations is given for sample 003 in Figure 11 which highlights that the constrained CPO model
 245 explains measured and CPO predicted seismic anisotropy to a high degree.

Observed and modelled velocity anisotropy for sample 007 are shown in Figure 12. Observed and modelled anisotropy are in excellent agreement, but both curves are clearly offset by $\sim 10^{\circ}$ from the predicted velocity variations from measured CPO in this sample.

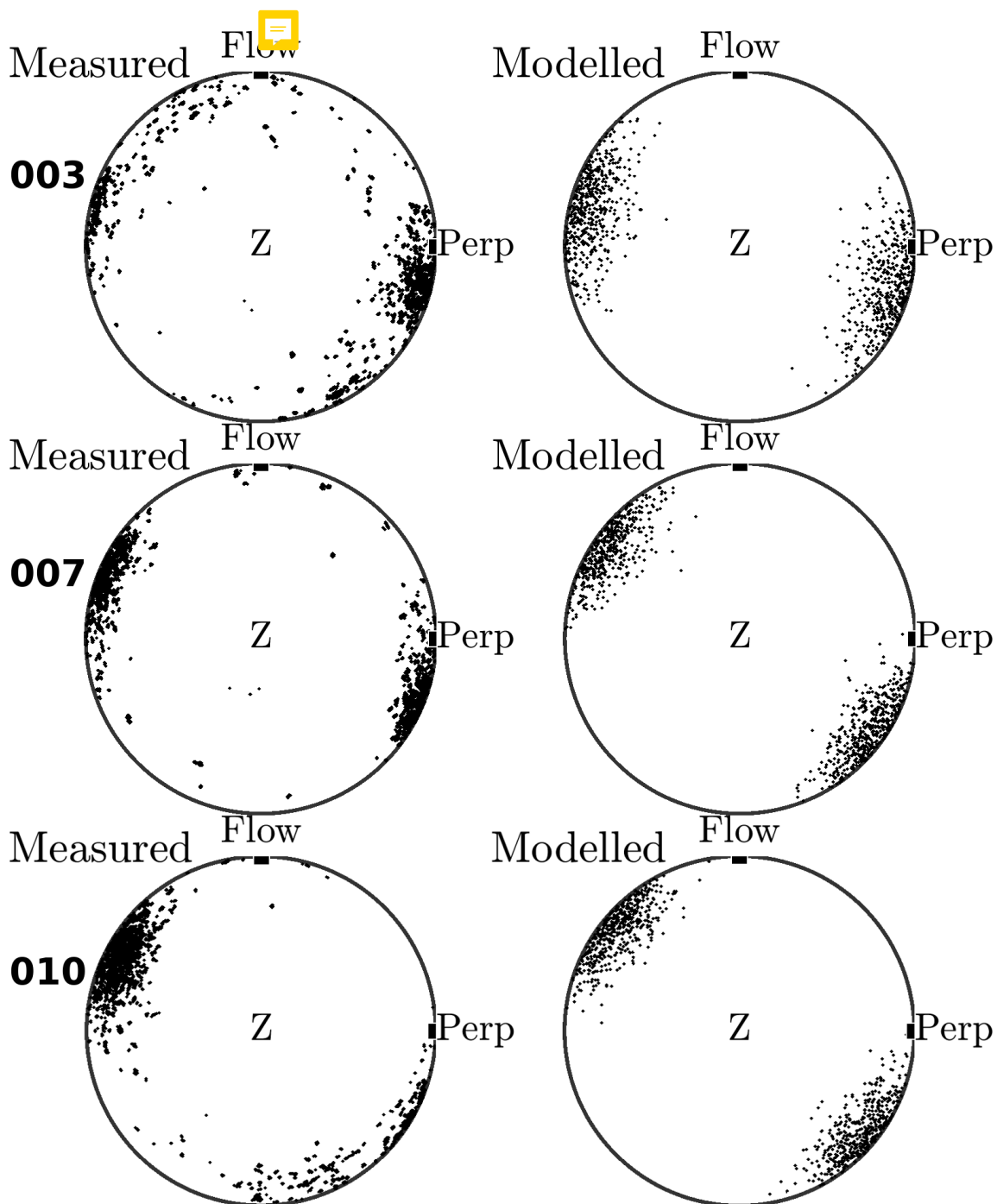


Figure 10. Measured (left) and modelled (right) CPO geometries. The VSP profile orientations of the “Flow” and “Perp” profiles are labelled. Top row: sample 003, middle row: sample 007, bottom row: sample 010.

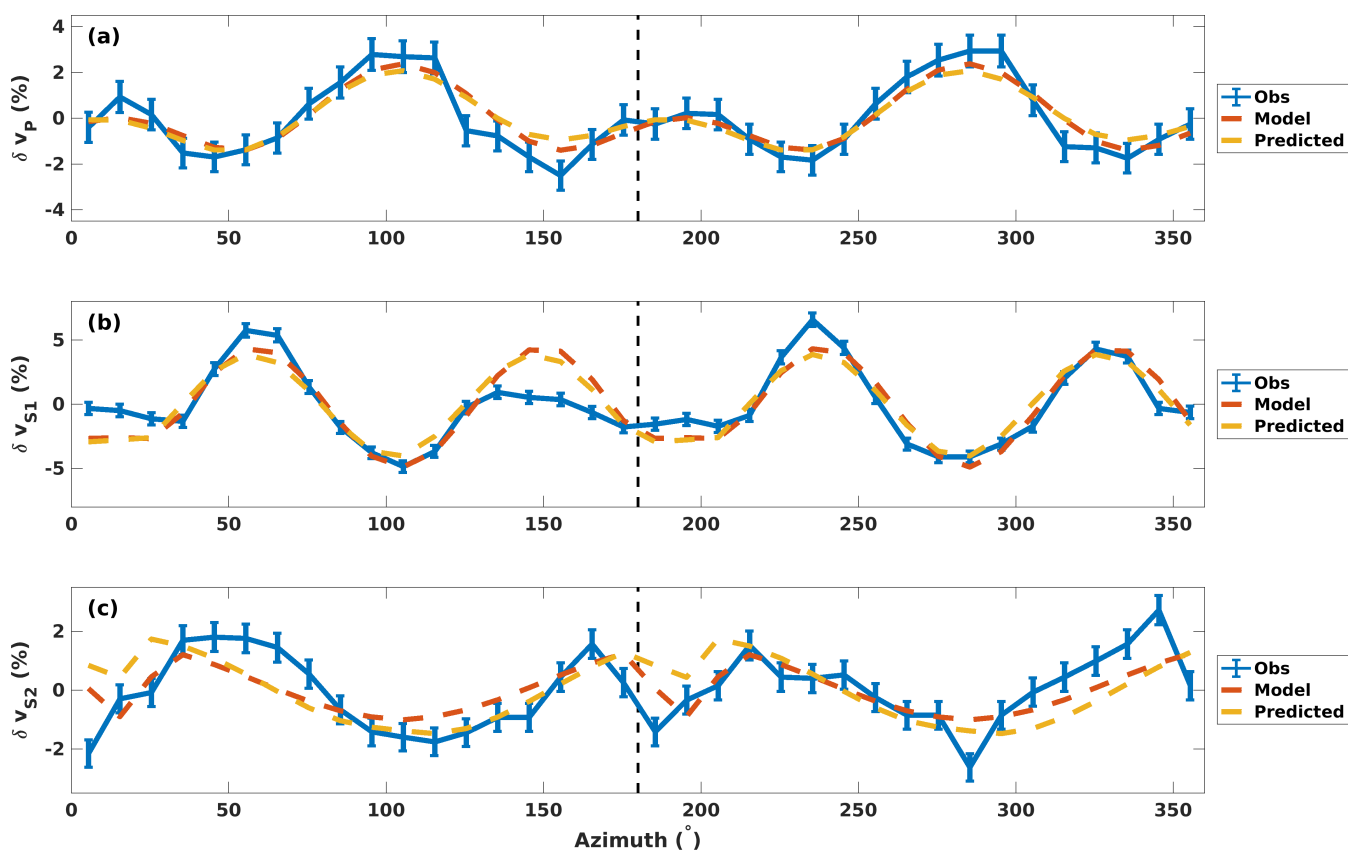


Figure 11. Observed, modelled and CPO-predicted anisotropy for sample 003. (a) δv_P (b) δv_{S1} (c) δv_{S2}

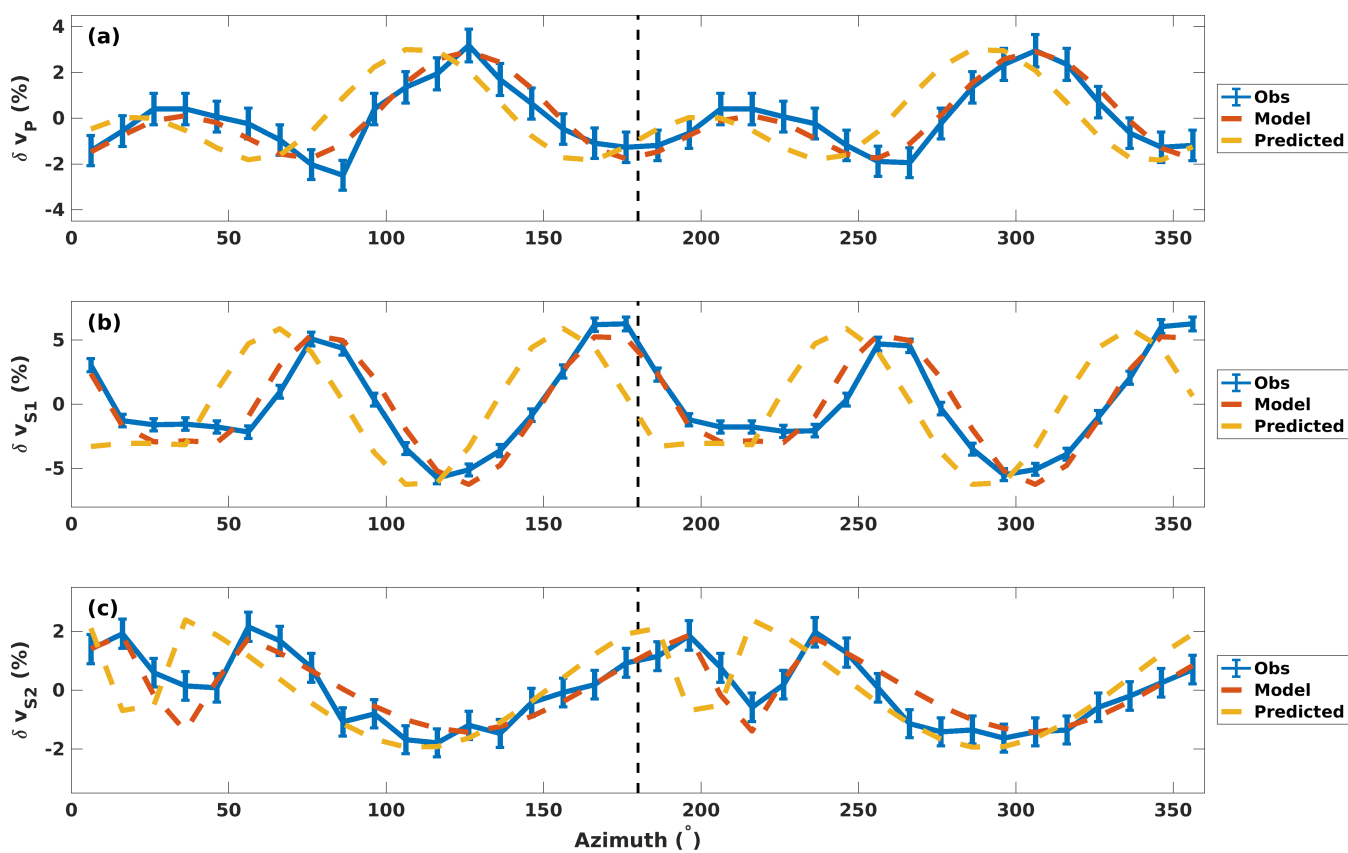


Figure 12. Observed, modelled and CPO-predicted anisotropy for sample 007. (a) δv_P (b) δv_{S1} (c) δv_{S2}



5 Discussion

250 5.1 Horizontal Cluster reconstruction

Both the VSP data and the ultrasonic data are best-matched by CPOs with cluster azimuths between 105° and 130° from the macroscopic ice flow direction at the site. This is consistent with CPO measurements made on core samples using EBSD analysis (Thomas et al., 2021). The agreement in model results between ultrasonic and seismic data bridges the two different scales at which these measurements are made. Ultrasonic and EBSD measurements that are made in ice core samples are shown
255 to be representative of anisotropy within the macroscopic volume that is sampled by the VSP survey.

The inter-sample variation of CPO cluster orientations inside the shallow ice at the site (Thomas et al., 2021) is also clearly visible in the ultrasonic velocity variation: Figure 4 shows that the ultrasonic velocities in the three samples follow highly similar patterns, which are however slightly offset between the individual samples. Different fast seismic directions in the studied samples are apparent in Figure 4, especially between sample 003 and samples 007/010. Consequently the CPO model
260 of 003 shows a different cluster azimuth than the models of samples 007 and 010 in Figure 10.

The c-axis maxima modelled from seismic anisotropies for samples 007 and 010 are rotated around the vertical axis relative to CPO measurements. This azimuthal difference between measured and modelled CPOs is best explained by small scale variation within the samples. There is a potential azimuthal error of up to about 3° in cutting and mounting samples for CPO measurement, and this error will primarily be a rotation around the core axis. Probably more important is the fact that the
265 locations of CPO and ultrasonic measurements for a sample do not coincide. As small-scale rotations of the c-axis maximum, around a vertical axis, are observed in the core (Thomas et al., 2021), a difference of a few 10s of mm in sample position could give a few degrees rotation of the c-axis maxima. Some sample locations, through the depth of the core, have a population of “oddly” oriented grains, in addition to a main c-axis maximum (Thomas et al., 2021), that would give rise to a rotation around a vertical axis of sample average acoustic anisotropy of $\sim 10^\circ$: areas with and without this orientation population can occur
270 within the same core section (Fig 9 in Thomas et al. (2021)).

The seismic VSP data records wavelengths that are larger than the scale of individual samples and therefore do not resolve a variation of cluster orientation at this scale. The CPO model informed by VSP velocities provides an averaging of any given variation in CPO properties over the entire sampled depth range. The CPO model found to best explain the VSP data is characterised by a slightly larger cone opening angle compared to results of the individual ultrasonic measurements and
275 therefore exhibiting slightly weaker anisotropy.

5.2 The role of studied seismic phase and survey geometry on CPO model ambiguity

The VSP seismic and ultrasonic datasets presented in this study have fundamentally different acquisition geometries which ultimately determine the observed velocity variation due to CPO. The constraint of CPO models from seismic anisotropy is consequently highly sensitive to the sampling geometry.

280 The ultrasonic data offer a dense sampling of velocities along azimuths in the horizontal direction. The given CPO type with horizontal c-axes clusters exhibits the largest magnitude of velocity variation in the horizontal plane, therefore this sampling



geometry results in high sensitivity to CPO parameters. The individual reconstructed CPO models using either v_P , v_{S1} or v_{S2} anisotropy are found to be consistent and also generally agree with measured CPO in core samples (see Figures 9 and 10). Periodicity of seismic anisotropy can however result in ambiguities: δv_P and δv_{S2} exhibit 180° periodicity and reconstruct
285 the CPO cluster's measured orientation without ambiguity. The cluster orientation reconstructed by $\chi(v_{S1})$ is also found to agree with measured orientation, however a misfit side minimum, offset by 90° azimuth, reduces confidence in the results. We propose to consider the information from velocity measurements of all phases that are available to avoid a side minimum. In this study this is done by forming the sum of individual misfits χ and selecting the model associated with the misfit minimum in this case.

290 The usefulness of velocity information from different seismic phases becomes even more apparent in a sparse sampling geometry, which is simulated here by downsampling of the multiazimuth ultrasonic dataset. Figure 13 presents model parameter results for sample 003 where, instead of 10° azimuth spacing between measurements, increments of 20° , 30° , 60° and 90° are used to inform CPO models. For each chosen new sampling interval, all possible downsampled datasets are considered. For example, an azimuth spacing of 20° allows two downsampled datasets to be created: one, where the first measurement is taken
295 at 0° azimuth and another one, where the first measurement is at 10° .

Models informed by $\chi(v_P)$ (Figure 13(a)) confirm the result of the full dataset if a coarser sampling of velocities with azimuths increments 20° , 30° or 60° is chosen. Models informed by multiazimuth measurements with 90° spacing show a large spread of CPO parameter results. Models informed by $\chi(v_{S1})$ and $\chi(v_{S2})$ (Figures 13(b)+(c)) agree for spacings of 20° and 30° , with larger spacings resulting in a wide scatter of model parameters. At 60° sampling, $\chi(v_{S1})$ reconstructs three
300 models at the realistic cluster orientation and three models at the 90° offset orientation associated with the misfit side minimum in Figure 9(b). The approach of using the sum of all misfits (Figure 13(d)) reduces the spread of found model parameters and finds realistic models for 20° and 30° spacing. For 60° spacing the cluster orientation angle is correctly found, however the cluster width poorly constrained. This is a clear improvement relative to the reconstructed model parameters in Figure 13(b)+(c) for 60° spacing. The results for 90° spacing are however still largely scattered and unrealistic.

305 Our downsampling analysis shows that an ideal survey geometry, which is in this case given by the sampling of a Horizontal Cluster CPO by horizontal velocity measurements, a realistic CPO model can be created from sampling in up to 30° steps regardless of the studied seismic phase. Observed scatter in model parameter results shows that aliasing becomes a critical effect for larger sampling intervals: the datasets with 20° and 30° sampling are much less sensitive to the choice of first sampled azimuth compared to the datasets with 60° and 90° spacing. The consideration of the full range of seismic velocity
310 information ($\chi(v_P) + \chi(v_{S1}) + \chi(v_{S2})$) can reduce scatter and aid to reconstruct a realistic CPO model from coarsely sampled data.

The VSP survey CPO modelling presents ambiguity in cluster orientation if only P-wave velocities are considered, as shown in Figure 6(a). The best-fitting model in this case does not match the CPO observations from the site, orienting the cluster at an azimuth that is offset by $\sim 45^\circ$ in anticlockwise direction from observed cluster orientations.

315 The difficulty to reconstruct a realistic CPO model from P-wave velocities in the VSP dataset is a consequence of poor azimuthal sampling. For the given CPO, the additional coverage of raypaths from a range of incidence angles provides little added

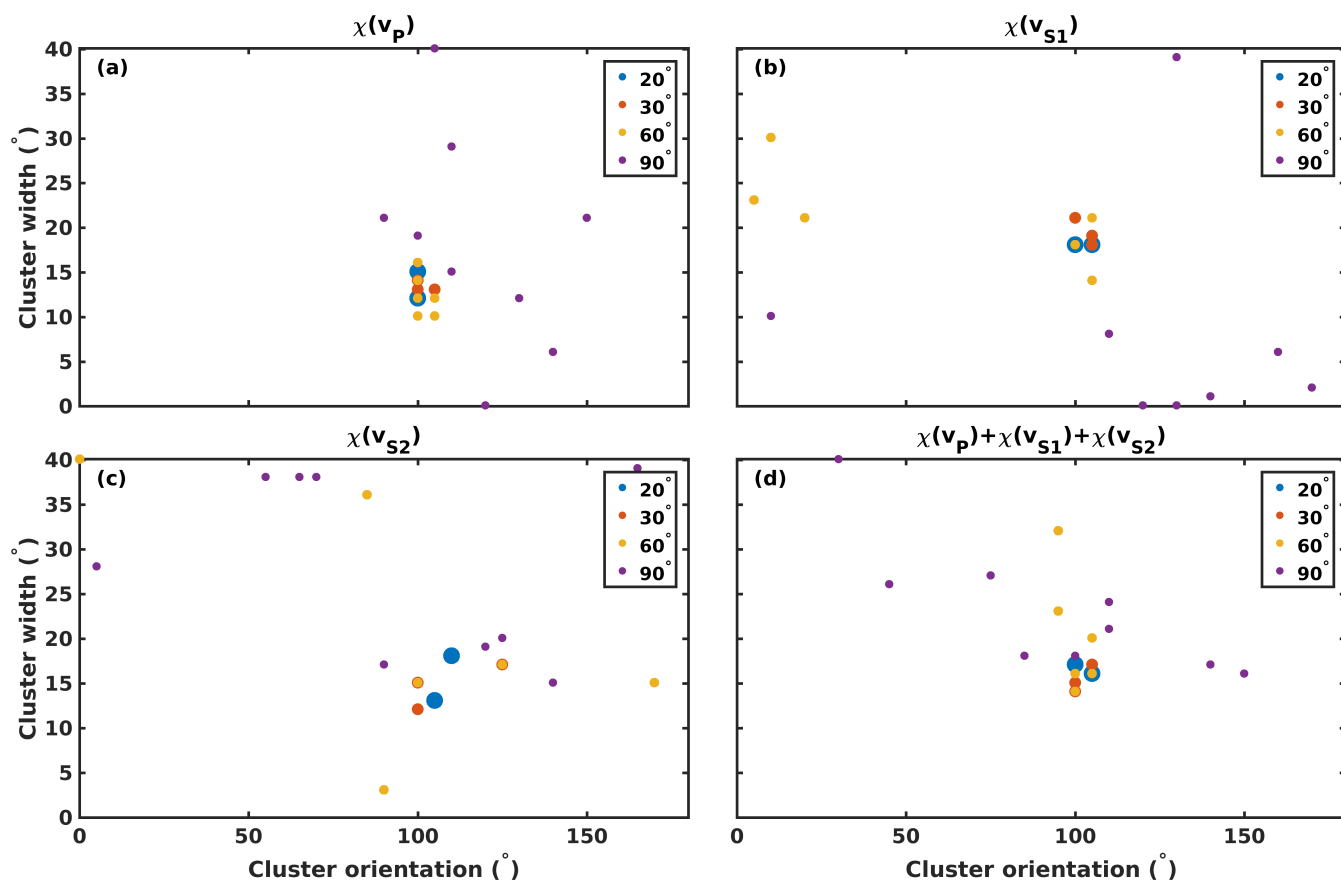


Figure 13. Parameter results using downsampled velocity measurements with azimuthal spacing of 20°, 30°, 60° and 90° for sample 003: (a) $\chi(v_P)$ (b) $\chi(v_{S1})$ (c) $\chi(v_{S2})$ (d) $\chi(v_P) + \chi(v_{S1}) + \chi(v_{S2})$

sensitivity compared to a dense azimuthal sampling of horizontal velocities, which characterises the ultrasonic measurements. The inclusion of P- and S-wave phase information mitigates this shortcoming of the VSP data by resolving the ambiguity in cluster orientation and identifying a CPO model which is in agreement with measured CPO. The study of all available seismic phases should therefore become standard in seismic CPO constraints in ice, rather than the commonly encountered focus on P-wave velocities.

For the Horizontal Cluster CPO, the variation of seismic velocities with incidence angle is highly dependent on the azimuth. Therefore, VSP data might be unable to constrain this CPO if azimuths with strong variation are not sampled. The difficulty to find a correct CPO model from VSP P-wave velocities could be a consequence of this problem, highlighted in Figure 7 by large errorbars relative to the overall v_P variation with incidence angle. The survey design could be improved by sampling of more profiles in finer azimuth spacing to increase confidence in the determined models. Furthermore, larger shot offsets should



be targeted to sample near-horizontal raypaths for the study of Horizontal Cluster CPOs, since the largest amplitude of the anisotropy signal is in the horizontal plane.



6 Conclusions

330 We have conducted a vertical seismic profile (VSP) experiment and laboratory ultrasonic experiments aimed at measuring the seismic anisotropy of ice from the lateral shear margin of the Priestley Glacier, Antarctica, and linking these data to measured crystallographic preferred orientations (CPOs).

P-wave and S-wave velocity anisotropy data from a ~ 50 m-scale, four-azimuth, walkaway-VSP experiment matches predictions from the horizontally clustered ice c-axes measured in the ice core from the borehole used for the VSP experiment. A
335 CPO model informed by P-wave data alone gives two equally likely orientations of the c-axis maximum azimuth, one of which is correct, and overestimates the strength of c-axes clustering. S-wave data alone or P-wave and S-wave data combined give a unique model best-fit that matches c-axis measurements.

Azimuthal ultrasonic P-wave and S-wave velocity measurements, made in 10° increments, on core samples from the borehole show the pattern of anisotropy with considerable detail. The anisotropy pattern matches the pattern predicted from the
340 CPO in the same sample. The anisotropy patterns in different samples are rotated through small angles relative to each other around the core axis: a pattern that matches direct CPO measurements.

The ultrasonic data have been degraded to larger azimuthal increments (20° , 30° , 60° and 90°) to explore how well these lower resolution data constrain the CPO responsible for velocity anisotropy. Increments of up to 30° constrain both the azimuthal orientation and intensity of horizontal c-axis alignment well. 60° increments constrain orientation. 90° increments do
345 not provide useful constraints.

Data availability. VSP seismic data, ultrasonic data and traveltimes are available at <https://figshare.com/s/8effdc8b145d79fc1788> (Lutz et al., 2021).

Author contributions. DJP and CLH lead the Priestley Glacier project. DJP and FL designed the seismic and ultrasonic experiments. FL collected the bulk of the ultrasonic data. HS collected the axial ultrasonic data. SF wrote MTEX code used to simulate CPOs. All authors
350 except CLH and SF were involved in seismic data collection in the field. FL wrote the manuscript in collaboration with DJP. All authors edited the manuscript.

Competing interests. The authors declare that there are no competing interests present.

Acknowledgements. We would like to acknowledge the logistics support from Antarctica New Zealand and field support from staff at Scott Base, Mario Zucchelli and Jang Bogo research stations. Funding for this research was provided by the Royal Society of New Zealand



355 Marsden Fund grant UOO1716 “Stretching ice to the limit: New flow laws for ice sheet modelling” and Korea Polar Research Institute project PE22430. FL is funded by a NZARI Early Career Researcher Seed Grant.



References

- Azuma, N. and Goto-Azuma, K.: An anisotropic flow law for ice-sheet ice and its implications, *Annals of Glaciology*, 23, 202–208, <https://doi.org/10.3189/S0260305500013458>, 1996.
- 360 Bentley, C. R.: Seismic Anisotropy in the West Antarctic Ice Sheet, pp. 131–177, American Geophysical Union, <https://doi.org/10.1029/AR016p0131>, 1971.
- Blankenship, D. D. and Bentley, C. R.: The crystalline fabric of polar ice sheets inferred from seismic anisotropy, *The Physical Basis of Ice Sheet Modelling*, 70, 17–28, 1987.
- Bouchez, J. and Duval, P.: The fabric of polycrystalline ice deformed in simple shear: experiments in torsion, natural deformation and
365 geometrical interpretation, *Texture, Stress, and Microstructure*, 5, 171–190, 1982.
- Budd, W. F., Warner, R. C., Jacka, T., Li, J., and Treverrow, A.: Ice flow relations for stress and strain-rate components from combined shear and compression laboratory experiments, *Journal of Glaciology*, 59, 374–392, <https://doi.org/10.3189/2013JoG12J106>, 2013.
- Diez, A., Eisen, O., Hofstede, C., Lambrecht, A., Mayer, C., Miller, H., Steinhage, D., Binder, T., and Weikusat, I.: Seismic wave propagation in anisotropic ice—Part 2: Effects of crystal anisotropy in geophysical data, *The Cryosphere*, 9, 385–398, 2015.
- 370 Drews, R., Wild, C. T., Marsh, O. J., Rack, W., Ehlers, T. A., Neckel, N., and Helm, V.: Grounding-Zone Flow Variability of Priestley Glacier, Antarctica, in a Diurnal Tidal Regime, *Geophysical Research Letters*, 48, e2021GL093853, <https://doi.org/https://doi.org/10.1029/2021GL093853>, 2021.
- Ershadi, M. R., Drews, R., Martín, C., Eisen, O., Ritz, C., Corr, H., Christmann, J., Zeising, O., Humbert, A., and Mulvaney, R.: Polarimetric radar reveals the spatial distribution of ice fabric at domes in East Antarctica, *The Cryosphere Discussions*, 2021, 1–34,
375 <https://doi.org/10.5194/tc-2020-370>, 2021.
- Faria, S. H., Weikusat, I., and Azuma, N.: The microstructure of polar ice. Part I: Highlights from ice core research, *Journal of Structural Geology*, 61, 2 – 20, <https://doi.org/https://doi.org/10.1016/j.jsg.2013.09.010>, microdynamics of Ice, 2014.
- Frezzotti, M., Tabacco, I. E., and Zirizzotti, A.: Ice discharge of eastern Dome C drainage area, Antarctica, determined from airborne radar survey and satellite image analysis, *Journal of Glaciology*, 46, 253–264, <https://doi.org/10.3189/172756500781832855>, 2000.
- 380 Gammon, P. H., Kieft, H., Clouter, M. J., and Denner, W. W.: Elastic Constants of Artificial and Natural Ice Samples by Brillouin Spectroscopy, *Journal of Glaciology*, 29, 433–460, <https://doi.org/10.3189/S0022143000030355>, 1983.
- Gerbi, C., Mills, S., Clavette, R., Campbell, S., Bernsen, S., Clemens-Sewall, D., Lee, I., Hawley, R., Kreutz, K., Hruby, K., and et al.: Microstructures in a shear margin: Jarvis Glacier, Alaska, *Journal of Glaciology*, p. 1–14, <https://doi.org/10.1017/jog.2021.62>, 2021.
- Gusmeroli, A., Murray, T., Clark, R. A., Kulesa, B., and Jansson, P.: Vertical seismic profiling of glaciers: Appraising multi-phase mixing
385 models, *Annals of Glaciology*, 54, 115–123, 2013.
- Hellmann, S., Grab, M., Kerch, J., Löwe, H., Bauder, A., Weikusat, I., and Maurer, H.: Acoustic velocity measurements for detecting the crystal orientation fabrics of a temperate ice core, *The Cryosphere*, 15, 3507–3521, <https://doi.org/10.5194/tc-15-3507-2021>, 2021.
- Hill, R.: The Elastic Behaviour of a Crystalline Aggregate, *Proceedings of the Physical Society. Section A*, 65, 349, <http://stacks.iop.org/0370-1298/65/i=5/a=307>, 1952.
- 390 Hruby, K., Gerbi, C., Koons, P., Campbell, S., Martín, C., and Hawley, R.: The impact of temperature and crystal orientation fabric on the dynamics of mountain glaciers and ice streams, *Journal of Glaciology*, 66, 755–765, <https://doi.org/10.1017/jog.2020.44>, 2020.
- Hudleston, P. J.: Structures and fabrics in glacial ice: A review, *Journal of Structural Geology*, 81, 1 – 27, <https://doi.org/https://doi.org/10.1016/j.jsg.2015.09.003>, 2015.



- Jackson, M. and Kamb, B.: The marginal shear stress of Ice Stream B, West Antarctica, *Journal of Glaciology*, 43, 415–426, 1997. <https://doi.org/10.3189/S0022143000035000>, 1997.
- Jordan, T., Schroeder, D., Elsworth, C., and Siegfried, M.: Estimation of ice fabric within Whillans Ice Stream using polarimetric phase-sensitive radar sounding, *Annals of Glaciology*, <https://doi.org/10.1017/aog.2020.6>, 2020.
- Journaux, B., Chauve, T., Montagnat, M., Tommasi, A., Barou, F., Mainprice, D., and Gest, L.: Recrystallization processes, microstructure and crystallographic preferred orientation evolution in polycrystalline ice during high-temperature simple shear, *The Cryosphere*, 13, 1495–1511, <https://doi.org/10.5194/tc-13-1495-2019>, 2019.
- Langway, C., Shoji, H., and Azuma, N.: Crystal Size and Orientation Patterns in the Wisconsin-Age Ice from Dye 3, Greenland, *Annals of Glaciology*, 10, 109–115, <https://doi.org/10.3189/S0260305500004262>, 1988.
- LeDoux, C. M., Hulbe, C. L., Forbes, M. P., Scambos, T. A., and Alley, K.: Structural provinces of the Ross Ice Shelf, Antarctica, *Annals of Glaciology*, p. 1–11, <https://doi.org/10.1017/aog.2017.24>, 2017.
- Lilien, D. A., Rathmann, N. M., Hvidberg, C. S., and Dahl-Jensen, D.: Modeling Ice-Crystal Fabric as a Proxy for Ice-Stream Stability, *Journal of Geophysical Research: Earth Surface*, 126, e2021JF006306, <https://doi.org/https://doi.org/10.1029/2021JF006306>, e2021JF006306 2021JF006306, 2021.
- Lutz, F., Eccles, J., Prior, D. J., Craw, L., Fan, S., Hulbe, C., Forbes, M., Still, H., Pyne, A., and Mandeno, D.: Constraining Ice Shelf Anisotropy Using Shear Wave Splitting Measurements from Active-Source Borehole Seismics, *Journal of Geophysical Research: Earth Surface*, 125, e2020JF005707, <https://doi.org/10.1029/2020JF005707>, e2020JF005707 10.1029/2020JF005707, 2020.
- Lutz, F., Prior, D. J., Still, H., Bowman, M. H., Boucinhas, B., Craw, L., Fan, S., Kim, D., Mulvaney, R., Thomas, R. E., and Hulbe, C. L.: Priestley Glacier seismic and ultrasonic datasets, <https://doi.org/10.17608/k6.auckland.17108639>, 2021.
- Mainprice, D.: Seismic Anisotropy of the Deep Earth from a Mineral and Rock Physics Perspective, vol. 2, pp. 437–492, <https://doi.org/10.1016/B978-044452748-6/00045-6>, 2007.
- Mainprice, D., Hielscher, R., and Schaeben, H.: Calculating anisotropic physical properties from texture data using the MTEX open-source package, *Geological Society, London, Special Publications*, 360, 175–192, <https://doi.org/10.1144/SP360.10>, 2011.
- Matsuoka, K., Furukawa, T., Fujita, S., Maeno, H., Uratsuka, S., Naruse, R., and Watanabe, O.: Crystal orientation fabrics within the Antarctic ice sheet revealed by a multipolarization plane and dual-frequency radar survey, *Journal of Geophysical Research: Solid Earth*, 108, <https://doi.org/https://doi.org/10.1029/2003JB002425>, 2003.
- Minchew, B. M., Meyer, C. R., Robel, A. A., Gudmundsson, G. H., and Simons, M.: Processes controlling the downstream evolution of ice rheology in glacier shear margins: case study on Rutford Ice Stream, West Antarctica, *Journal of Glaciology*, 64, 583–594, <https://doi.org/10.1017/jog.2018.47>, 2018.
- Monz, M. E., Hudleston, P. J., Prior, D. J., Michels, Z., Fan, S., Negrini, M., Langhorne, P. J., and Qi, C.: Full crystallographic orientation (*c* and *a* axes) of warm, coarse-grained ice in a shear-dominated setting: a case study, Storglaciären, Sweden, *The Cryosphere*, 15, 303–324, <https://doi.org/10.5194/tc-15-303-2021>, 2021.
- Mouginot, J., Rignot, E., and Scheuchl, B.: Continent-Wide, Interferometric SAR Phase, Mapping of Antarctic Ice Velocity, *Geophysical Research Letters*, 46, 9710–9718, <https://doi.org/10.1029/2019GL083826>, 2019.
- Picotti, S., Vuan, A., Carcione, J. M., Horgan, H. J., and Anandkrishnan, S.: Anisotropy and crystalline fabric of Whillans Ice Stream (West Antarctica) inferred from multicomponent seismic data, *Journal of Geophysical Research: Solid Earth*, 120, 4237–4262, 2015.



- 430 Qi, C., Prior, D. J., Craw, L., Fan, S., Llorens, M.-G., Griera, A., Negrini, M., Bons, P. D., and Goldsby, D. L.: Crystallographic preferred orientations of ice deformed in direct-shear experiments at low temperatures, *The Cryosphere*, 13, 351–371, <https://doi.org/10.5194/tc-13-351-2019>, 2019.
- Sayers, C. M.: Increasing contribution of grain boundary compliance to polycrystalline ice elasticity as temperature increases, *Journal of Glaciology*, 64, 669–674, <https://doi.org/10.1017/jog.2018.56>, 2018.
- 435 Thomas, R. E., Negrini, M., Prior, D. J., Mulvaney, R., Still, H., Bowman, M. H., Craw, L., Fan, S., Hubbard, B., Hulbe, C., Kim, D., and Lutz, F.: Microstructure and Crystallographic Preferred Orientations of an Azimuthally Oriented Ice Core from a Lateral Shear Margin: Priestley Glacier, Antarctica, *Frontiers in Earth Science*, 9, 1084, <https://doi.org/10.3389/feart.2021.702213>, 2021.
- Truffer, M. and Echelmeyer, K. A.: Of isbræ and ice streams, *Annals of Glaciology*, 36, 66–72, <https://doi.org/10.3189/172756403781816347>, 2003.
- 440 Vélez, J. A., Tsoflias, G. P., Black, R. A., van der Veen, C. J., and Anandakrishnan, S.: Distribution of preferred ice crystal orientation determined from seismic anisotropy: Evidence from Jakobshavn Isbræ and the North Greenland Eemian Ice Drilling facility, Greenland, *Geophysics*, 81, 111–118, <https://doi.org/10.1190/geo2015-0154.1>, 2016.
- Wüstefeld, A., Al-Harrasi, O., Verdon, J. P., Wookey, J., and Kendall, J. M.: A strategy for automated analysis of passive microseismic data to image seismic anisotropy and fracture characteristics, *Geophysical Prospecting*, 58, 755–773, <https://doi.org/10.1111/j.1365-2478.2010.00891.x>, 2010.
- 445